Journal of Materials Chemistry A

PAPER

View Article Online
View Journal | View Issue

Cite this: J. Mater. Chem. A, 2015, 3, 23120

Gold aerogel supported on graphitic carbon nitride: an efficient electrocatalyst for oxygen reduction reaction and hydrogen evolution reaction†

Manas Kumar Kundu, Tanmay Bhowmik and Sudip Barman*

Received 26th August 2015
Accepted 1st October 2015

DOI: 10.1039/c5ta06740e

www.rsc.org/MaterialsA

Fabrication of a high surface area interconnected porous network of metallic nanomaterials is important for their applications in various fields such as catalysis, sensors, and electrochemistry. Here we report a facile bottom up synthesis of high surface area and porous gold aerogel supported on carbon nitride sheets (CN_x). The reduction of $HAuCl_4$ in the presence of carbon nitride nanosheets using sodium borohydride and ultrasonic treatment produces gold aerogel supported on carbon nitride (Au–aerogel–CN_x). When the reduction of $HAuCl_4$ in the presence of CN_x nanosheets was performed using only ultrasonication, highly dispersed ultrasmall (~2 nm) gold nanoparticles on CN_x sheets (AuNPs–CN_x) were formed. The Au aerogel supported on CN_x sheets was well characterized by powder X-ray diffraction, tunneling electron microscopy, selected area electron diffraction, energy dispersive X-ray spectroscopy, scanning electron microscopy, UV-visible and X-rayphotoelectron spectroscopic methods. The Au–aerogel–CN_x and AuNPs–CN_x composites exhibited superior electrocatalytic activity towards oxygen reduction reaction (ORR) in alkaline and acidic media. The Au–aerogel–CN_x composite showed ORR onset potentials at 0.92 V and 0.43 V (*vs.* RHE) in 0.5 M KOH and H_2SO_4 solution. The four electron oxygen reduction process occurred at these supported catalysts in both alkaline and acidic media. In alkaline (KOH) medium the onset potential at Au–aerogel–CN_x was more positive (~30 mV) than that of commercial Pt/C catalyst. The composites displayed excellent methanol tolerance and comparable durability with commercial Pt/C. Furthermore, the Au–aerogel–CN_x composites exhibited high catalytic activity for the hydrogen reduction reaction (HER) with a small onset potential of −30 mV and a Tafel slope of 53 mV dec^{-1} in acidic medium. At a small Au loading of 0.130 mg cm^{-2}, this catalyst also exhibits a current density of 10 mA cm^{-2} at a low overpotential of −185 mV with excellent stability. The ORR and HER performances on porous Au–aerogel–CN_x composites were better than those of the AuNPs–CN_x catalyst and commercial flat gold electrode. The superior ORR and HER activities at the Au–aerogel–CN_x composite originated from the unique synergistic effects between the porous Au network and carbon nitride (CN_x) support.

Introduction

Porous materials have attracted tremendous attention in the last few years due to their exceptionally high catalytic activity,[1–3] electrical conductivity[4] and mechanical properties.[5] These properties arise due to their ability to interact with the atoms or ions or molecules throughout the bulk of the material, and not only on their surfaces. In the last decade porous metallic network structures have gained tremendous attention for their various kinds of biological sensing applications[6,7] and catalytic[3] and electrocatalytic applications.[8] Metal aerogels are a new type of porous solid materials that have extremely low density, high porosity, high surface area, high electrical conductivity and catalytic properties. The properties of nanoparticles such as catalytic activities are retained in the metal aerogel and it may thus bridge the gap between nanomaterials and macro-materials. It was reported that the properties of some of the metal aerogels are superior to those of metal nanoparticles because of the combined effects of nanoparticles in the aerogel.[9] Since the discovery of aerogels in 1963 by Kistler,[10] enormous efforts have been taken to synthesise various aerogels. Several approaches are available in the literature for the synthesis of different non-metal aerogels such as carbon aerogels[11] and silica aerogels,[12] organic–inorganic hybrid aerogels,[13] metal oxide aerogels,[14] and metal chalcogenide aerogels.[15] But only few methods are available for the production of metal aerogels.[8,16–18] For example, Eychmüller and coworkers[8,16] have

School of Chemical Sciences, National Institute of Science Education and Research (NISER), Bhubaneswar, Orissa 751 005, India. E-mail: sbarman@niser.ac.in; Fax: +91 674 2304070; Tel: +91 674 2304061

† Electronic supplementary information (ESI) available: TEM images, TGA analysis, IR spectra, deconvoluted XPS spectra of CVs of ORR in acidic medium. See DOI: 10.1039/c5ta06740e

reported the synthesis of monometallic, bi-metallic and composite aerogels based on the controlled aggregation of metal nanoparticles using controllable destabilization and spontaneous gelation methods. Leventis and his co-workers[17,18] developed methods for the synthesis of different metallic (Fe, Cu, Ni, Co) aerogels by nanosmelting (sol–gel method) of hybrid polymer–metal oxide composites. A combustion method for the synthesis of porous metallic aerogels was also reported by Tappan *et al.*[19] The synthesis of metallic aerogels supported on a two dimensional conducting support and their catalytic applications have not been reported so far.

The synthesis of supported nanostructured compounds and studies on their catalytic properties have attracted great attention of the scientific community recently since catalytic supports not only stabilize the nanoparticles, but also enhance their catalytic activities in some cases. For example, supported gold nanoparticles display superior catalytic activity for various chemical reactions,[20] such as low temperature catalytic combustion, partial oxidation of organic molecules, reduction of oxygen and hydrogen peroxide. It is also well known that the catalytic activity of gold catalysts depends not only on the size of the nanoparticles, but also the nature of the support materials and preparation methods of the catalysts are also important for their superior catalytic activity. The remarkably high catalytic oxidation of CO over gold nanoparticles dispersed on various metal oxide catalysts was explained by the synergic effect between gold nanoparticles and metal oxides.[21–23] Graphene has already become a promising candidate as a two dimensional support for different nanoparticles due to its unique properties.[24] Another 2D material, graphitic carbon nitride (g-C_3N_4), which has a similar structure to that of graphene, is a promising support for various nanomaterials. Graphene/g-C_3N_4 supported metal or semiconductor nanoparticles have proven to be effective materials for photocatalysis,[25–27] catalysis[2,28] and biosensor applications.[29,30] Though C_3N_4 supported nanoparticles have been reported by several groups,[26,27,30] C_3N_4 or other 2D material supported metal Au aerogels have not been reported so far. However, few self-supported metal aerogels and their applications are available in the literature. For example, the synthesis of Pt–aerogels and Pt based bi-metallic aerogels was reported for ORR.[31] Pd–aerogels were reported for formic acid oxidation[32] and ethanol oxidation.[33]

The concern about energy shortage and environmental pollution is rising due to the use of fossil fuels; there is thus always need for alternate renewable green sources of energy.[34,35] Electrochemical energy generation by means of fuel cells and electrochemical water splitting is one of the most viable green approaches for energy generation. The oxygen reduction reaction (ORR) and hydrogen evolution reaction (HER) are the two important processes that are involved in fuel cells and electrochemical water splitting. Without a suitable catalyst, both these reactions (HER and ORR) show sluggish kinetics. Platinum is the best known catalyst for both processes. But the high cost and scarcity of platinum prevent its wide spread commercialization. It is important to develop non-platinum based ORR active cathodes for commercialization of fuel cells. Enormous efforts have been made during the past decades in finding an economically viable, novel and superior catalyst for this purpose. Recently, noble metal nanoparticles have been found to be highly promising electrocatalysts due to their high surface area and cost-effective production since only small amounts of metals are used in their synthesis. Bulk gold metal shows moderate ORR activity and its activity depends on the size of the nanoparticles. For example, Crompton and co-workers[36] showed that ultra-small (1.5–2 nm) citrate capped gold nanoparticles act as a negative catalyst for ORR in comparison to the Au macro-electrode. It was also reported by the same authors[37] that 17–40 nm AuNPs showed comparable ORR properties with those of the Au electrode and H_2O_2 was the final product due to the two electron reduction of oxygen. M. Bron[38] claimed that surface specific activity and the number of electrons transferred in the ORR process of carbon black stabilized AuNPs are independent of each other resulting in nanoparticles of different sizes (2.2–42.3 nm). T. Inasaki *et al.*[39] reported that SA increases with decreasing particle size and the number of electrons transferred per O_2 molecule also increases. S. Guerin *et al.*[40] found that the specific activity towards ORR decays rapidly with decreasing particle size below 3 nm. Although several reports on the ORR activity of Au nanoparticles are available, they are still less in number than those available for platinum.

Electrolysis of water to generate hydrogen through the HER process in acidic medium, *i.e.* electro-catalytic reduction of protons to molecular hydrogen, shows a promising approach to produce clean energy.[34,35] An efficient HER catalyst is required to produce large cathodic current densities at low overpotentials.[41] Research efforts are underway to find suitable hydrogen evolution catalysts based on more economical materials such as Ni Based catalysts,[42,43] Mo based catalysts,[41,44,45,46] other transition metal phosphides[47,48] *etc.*, which may replace the expensive Pt catalysts. The gold surface shows moderate HER activity. Although some reports of HER on gold are available, these are mostly dedicated to either the influence of surface structure[49] on the HER rates or effects of organic molecules on HER performances.[50] J. Perez *et al.*[51] reported pronounced structural sensitivity of the Au crystal face and they showed that catalytic activity decreases in the sequence Au(111) < Au(100) < Au(110). Negative HER activity of small (1–2 nm) AuNPs was also reported recently.[36]

Herein, we report the facile synthesis of gold aerogel supported on thin carbon nitride sheets (Au–aerogel–CN_x) and its applications in oxygen reduction (ORR) and hydrogen evolution (HER) reactions. Highly porous interconnected metal nanoparticle networks are formed on the CN_x support due to the reduction of $HAuCl_4$ in the presence of g-CN_x nanosheets with $NaBH_4$ and ultrasound treatment, whereas only ultrasonic reduction (without $NaBH_4$) produces highly dispersed ultrasmall (~2 nm) gold nanoparticles supported on CN_x sheets (AuNPs–CN_x). The Au–aerogel–CN_x and AuNPs–CN_x composites exhibited superior electrocatalytic activities towards ORR in acidic and basic media. The ORR activity of the Au aerogel composite in basic medium is better than that of commercial Pt/C whereas it is lower than that of Pt/C in acidic medium, but better than that of previously reported gold metal based electrocatalysts. Oxygen reduction in acidic and basic media occurs

via a 4-electron pathway at both AuNPs and Au aerogel supported CN_x catalysts. Furthermore, these two composites also showed superior hydrogen evolution activity in acidic medium. The morphology dependent HER behaviour of Au composites was observed in acidic media; the Au–aerogel–CN_x composite showed the best performance and the flat gold electrode displayed the poorest performance. The Au–aerogel CN_x catalyst exhibited an onset potential of −30 mV, current density of 10 mA cm^{-2} at a small HER overpotential of −185 mV and a Tafel slope of 53 mV dec^{-1} with excellent durability. The superior HER and ORR activities of the Au–aerogel supported CN_x composite are explained based on the synergetic effects of the CN_x support and porous gold and the strong catalyst–support interaction.

Experimental section

Preparation of g-CN_x

Formamide was used as the precursor for synthesizing carbon nitride quantum dots by a microwave mediated method.[52,53] Typically 30 ml of formamide was heated using a microwave synthesizer for 2 h at 180 °C. The resulting brown coloured solution was evaporated at 180 °C in a rotary-evaporator to obtain a bulk amount of a black product. This product was washed with water, filtered and vacuum dried to obtain dry, solid g-CN_x.

Preparation of the Au–aerogel–CN_x composite

5 mg of the as-prepared g-CN_x was dispersed in 3 ml of water by sonication for 10 min. The aqueous solution of $HAuCl_4$ was also prepared in a separate vial. These two solutions were mixed together followed by sonication for 10 minutes. Then solid $NaBH_4$ was added and the mixture was subjected to ultrasound treatment with ~28 kHz frequency for 3 hours at 400 watt. After ultrasound treatment the freshly formed solid product was separated by centrifugation at 8000 rpm for 10 minutes. After washing with water, Au aerogel supported CN_x products were dried under vacuum. 0.162 mmol $HAuCl_4$ and 0.53 mmol $NaBH_4$ solutions were used for the synthesis of 82 wt% Au–aerogel–CN_x whereas 0.235 mmol of $HAuCl_4$ and 0.79 mmol $NaBH_4$ solutions were used for 92 wt% Au–aerogel–CN_x. Gold nanoparticles supported on CN_x were produced by carrying out only the ultrasonic treatment of $HAuCl_4$ (0.147 mmol) in the presence of CN_x sheets (5 mg) without the use of any reducing agent.[26]

Preparation of Au–aerogel–CN_x/GC and AuNPs–CN_x/GC electrodes

A glassy carbon electrode was polished with 1.0, 0.1 and 0.05 mm alumina slurry on Buehler microcloth polishing cloth. After rinsing, the electrode was sonicated in distilled water for about 10 min. 1 mg of the synthesized composite was dissolved in 1 ml water to make a stock solution. 15, 11, and 10 μl of aqueous stock solution were evaporated on the cleaned glassy carbon electrode to prepare AuNPs–CN_x/GC and Au–aerogel–CN_x/GC electrodes to maintain a constant amount of Au in every electrode. ORR was conducted in both alkaline and acidic media with the help of linear sweep voltammetry (LSV) and cyclic voltammetry (CV) measurements by using oxygen saturated 0.5 M H_2SO_4 and KOH at 100 mV sec^{-1} scan rate. For HER analysis LSV measurement was carried out using nitrogen saturated 0.5 M H_2SO_4 at 10 mV sec^{-1} scan rate.

Results and discussion

Characterization of Au aerogel composites

The powder X-ray diffraction (p-XRD) patterns of g-CN_x, AuNPs–CN_x, and Au–aerogel–CN_x nanocomposites are shown in Fig. 1. The peak positioned at a 2θ value of 27.30 corresponds to the (002) plane of g-CN_x with an interlayer *d*-spacing of 3.27 Å which was reported previously by our group.[52,53] The five additional well-resolved peaks of Au composites located at 2θ values of 38.20, 44.40, 64.50, 77.540 and 81.80 can be indexed as the (111), (200), (220), (311) and (222) reflection planes respectively for pure face centred cubic (f.c.c.) Au nanoparticles[54] (JCPDS no. 04-0784). The p-XRD pattern of the Au–aerogel–CN_x composite was further studied by Scherrer analysis (see the ESI† for details). The most intense peak positioned (2θ) at 38.20 was used to calculate the size of the Au–aerogel in the composite and the gold nanoparticle size of ~8 nm was calculated from the Scherrer analysis. Tunnelling electron microscopy (TEM) and field emission scanning electron microscopy (FESEM) were used to study the morphology of the Au–aerogel network supported on CN_x sheets. TEM samples were prepared by the evaporation of 10 μl aqueous solution of the Au aerogel–CN_x composite on a TEM grid. Fig. 2a shows the TEM image of two dimensional thin CN_x sheets which were formed on evaporation of g-CNQDs. Ultrasound treatment of $HAuCl_4$ and CN_x sheets produces the AuNPs–CN_x composite. As shown in Fig. 2b and S1a,† good nearly ordered distribution of 1.0–2.5 nm sized gold nanoparticles on CN_x sheets was observed after ultrasound treatment. The formation of noble metal particles on the surface of CN_x sheets resulting from ultrasound treatment without the use of a reducing agent was reported by our group

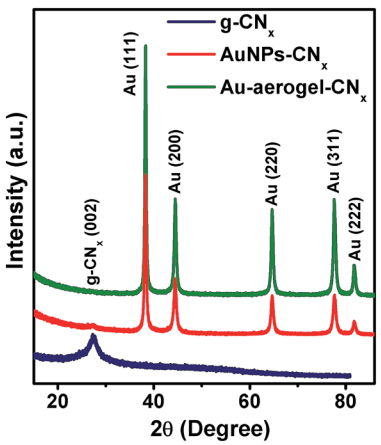

Fig. 1 p-XRD of g-CN_x, AuNPs–CN_x and the Au–aerogel–CN_x composite.

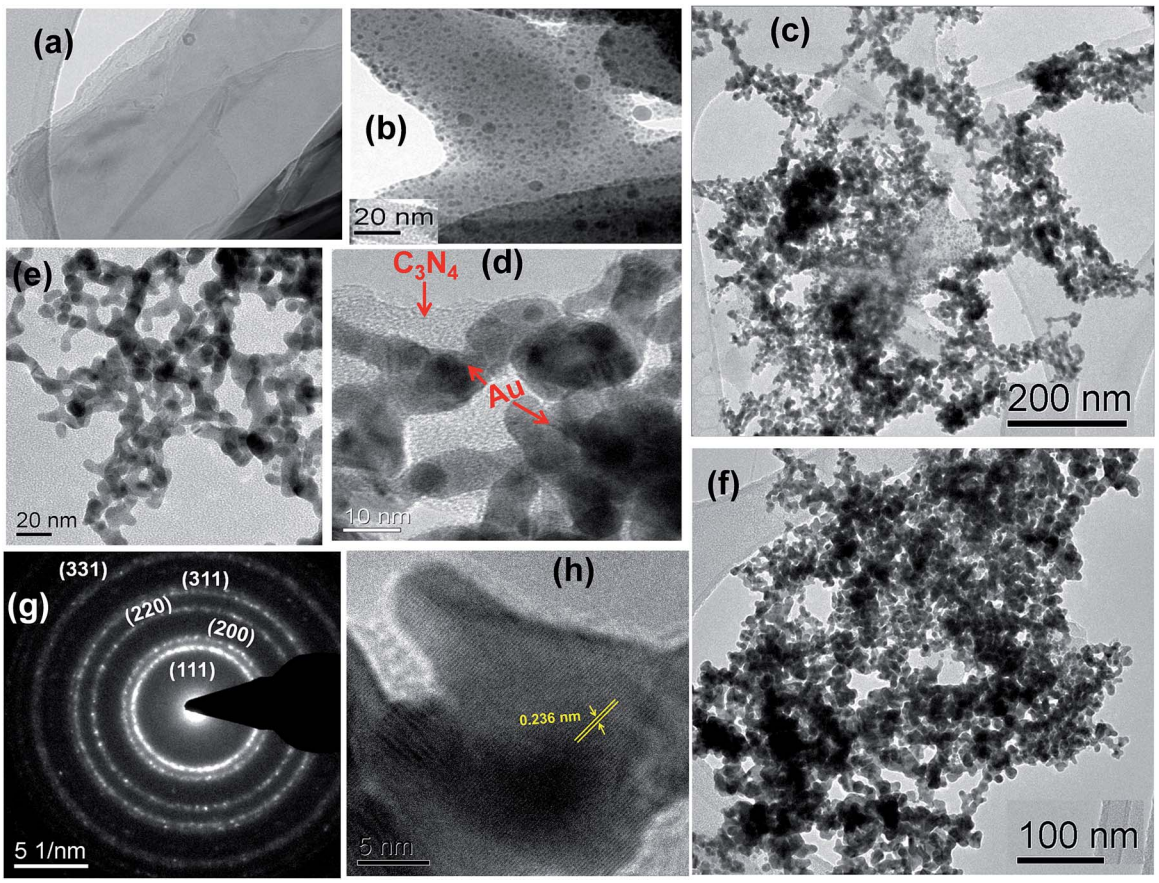

Fig. 2 TEM images of (a) g-CN_x sheets, (b) AuNPs on CN_x (AuNPs–CN_x composite) showing highly dispersed ultrasmall AuNPs on the CN_x sheets: (c and f) low resolution TEM images of the Au–aerogel supported on CN_x showing porous morphology. (d and e) Mid-resolution TEM images of the Au–aerogel showing interconnected Au nanochains and the CN_x support. (g) SAED images taken from (c). (h) HRTEM images of Au–aerogel–CN_x showing preferential growth along the Au(111) plane.

recently.[26] When the reduction of $HAuCl_4$ in the presence of CN_x sheets was performed using $NaBH_4$ along with the ultrasound treatment, Au–aerogel supported on CN_x sheets was produced. Some representative TEM images of the Au–aerogel supported on CN_x sheets are shown in Fig. 2c–f and S1(d–i) (ESI†). In all these images, the ultrathin Au nanowires are interconnected to form three dimensional network-like structures with a large number of open pores. The Au aerogel with a porous structure is supported on CN_x sheets, which is clearly visible in Fig. 2d and S1h (ESI†). The nanochains have a uniform diameter of about 8–10 nm. The coalescence of the initial spherical particles into a chain structure is quite obvious in the TEM images. The assembly of 6–8 nm size nanoparticles supported on CN_x sheets is also seen (Fig. S1f, ESI†), but their abundance is low. Since the size of independent nanoparticles and the diameter of the nanochains are more or less similar, it can be concluded that the aerogel is formed directly from the colloidal particles by the fusion of the nanoparticles and no pre-agglomeration occurs. The SAED image of the Au aerogel is shown in Fig. 2g suggesting a polycrystalline structure, as shown in Fig. 2d. The interlayer spacings calculated from the SAED image are found to be 2.36, 2.03, 1.44, 1.22, and 0.946 Å which correspond to the (111), (200), (220), (311) and (331) planes of the fcc gold lattice. This is in good agreement with p-XRD studies (see Fig. 1) of Au-composites. The HRTEM images as shown in Fig. 2h and S1i (ESI†) clearly show the lattice fringes with a d spacing of 2.36 Å corresponding to the (111) plane of face centred cubic gold. The orientations of these lattice fringes are similar. This suggests that the gold aerogel generally grows along the Au(111) planes. From the TEM analysis it can be concluded that the interconnected Au network was formed due to ultrasound treatment in a mixture of $HAuCl_4$, CN_x and $NaBH_4$.

To understand the formation mechanism of Au–aerogel on CN_x sheets, the structural morphologies of several compounds, prepared by varying the amount of $NaBH_4$, were examined using TEM. When no $NaBH_4$ was used, only ultrasonic treatment of $HAuCl_4$ and CN_x yielded nearly ordered, highly dispersed AuNPs of size ~2 nm on CN_x sheets, as shown in Fig. 2b and S1a.† The size of these particles was between 1.0 and 2.5 nm with a mean diameter of 2 nm. On addition of a small amount of $NaBH_4$ (0.10 mmol) during the synthesis process, highly dispersed gold nano-dots of size less than 1 nm on CN_x were formed and some nanochains with single or few branches were also visible (Fig. S1b,c in ESI†) indicating the initiation of aerogel formation. Since the amounts of CN_x nano-sheets and $HAuCl_4$ used were the same, varying only the amount of $NaBH_4$ in the

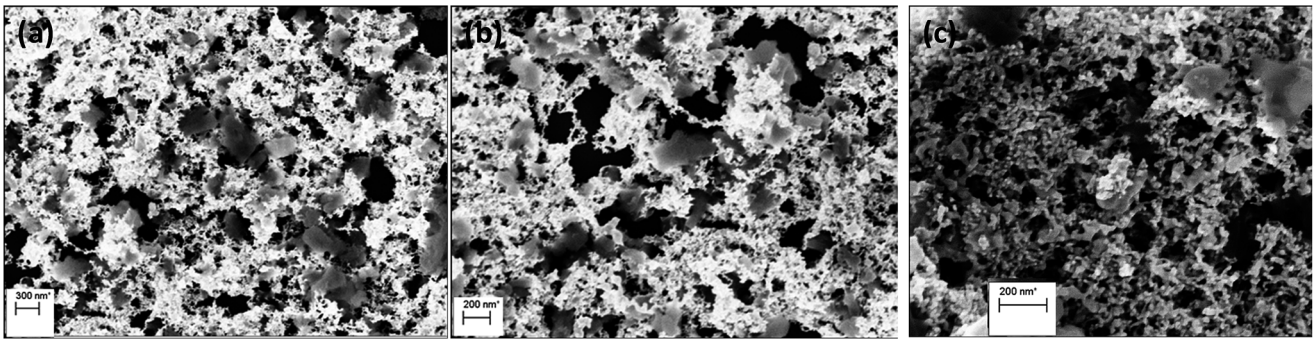

Fig. 3 FESEM images of Au–aerogel–CN_x showing highly porous morphologies of interconnected nanoparticles.

synthesis of these two Au–aerogel composites, the same amount of Au atoms was produced due to ultrasonication with or without $NaBH_4$. Some of the gold atoms were utilized for the formation of gold nanochains when the synthesis was carried out in the presence of a small amount of $NaBH_4$. This explains why gold nanoparticles (less than 1 nm) produced with a small amount $NaBH_4$ are smaller than those produced (2 nm) when ultrasonication was performed without employing any reducing agent. On the other hand, as shown in Fig. 2d–f, a highly porous, interconnected gold nanochain network structure (aerogel) supported on CN_x sheets was formed when sufficient $NaBH_4$ (0.79 mmol solution) was added during the synthesis process. These TEM images clearly show that the aerogels were composed of ultrathin gold nanochains with a diameter of 8–10 nm. The ultrasonication of $HAuCl_4$ without $NaBH_4$ produced gold atoms (nanoparticles) at a low pace due to the slow reduction of $HAuCl_4$, and AuNPs were physically adsorbed on the surface of CN_x sheets. Since the fast reduction of $HAuCl_4$ with $NaBH_4$ produced a large number gold atoms in a very short time, nucleation and uncontrolled growth of nanoparticles occurred on CN_x sheets to form a porous network of gold on the CN_x support. The exact amount of gold loading in Au–aerogel–CN_x was determined by the thermogravimetric analysis (TGA) method. TGA curves (Fig. S2†) show 82 wt% loading of Au on Au–aerogel supported CN_x whereas the Au loading is 58% in the AuNPs–CN_x composite. In order to achieve higher Au loading samples were also prepared with a higher amount of $HAuCl_4$ and $NaBH_4$ using a constant amount of CN_x sheets. The highest loading we could achieve was 92 wt% gold when 0.235 mmol $HAuCl_4$ and 0.79 mmol $NaBH_4$ were used for the synthesis. The amount of gold loading in these catalysts was also determined by inductively coupled plasma optical emission spectrometry (ICP-OES) and the concentrations of carbon and nitrogen were determined by EDX and XPS analysis. The exact wt% of Au present in Au–aerogel–CN_x and AuNPs–CN_x composite was 85.4 and 55.9 respectively. The carbon : nitrogen ratio in Au–aerogel–CN_x and AuNPs–CN_x was 1.25 : 1 and 1 : 1.1 respectively. Fig. 2f and S1g (ESI†) represent the Au–aerogel–CN_x composite with 92 wt% Au loading. The width of the nanochains is almost the same as that of the 82 wt% loading sample, but the pore size becomes small due to the large number of interconnections between nanochains forming a highly porous Au network on the CN_x support and the nanoparticles are clearly visible in the nanochains since a large amount of the Au precursor was used. The 82 wt% and 92 wt% Au loading in the Au–aerogel supported CN_x composite is abbreviated as Au–aerogel(1)–CN_x and Au–aerogel(2)–CN_x respectively. FESEM images (Fig. 3a–c) have also been taken to study the surface morphology of the composite on a silicon substrate. FESEM samples were prepared by the evaporation of 30 μl stock solution with 0.5 mg ml^{-1} concentration on Si wafer. In the FESEM images the interconnected porous network with an ultrathin wire-like structure with many bifurcations is clearly visible.

Fig. 4a shows the UV-visible spectrum of aqueous solution of g-CN_x and Au–aerogel–CN_x. The strong surface plasmon peak at 540 nm for the Au–aerogel–CN_x compound suggests the presence of the Au nanostructure. X-ray photoelectron spectroscopy

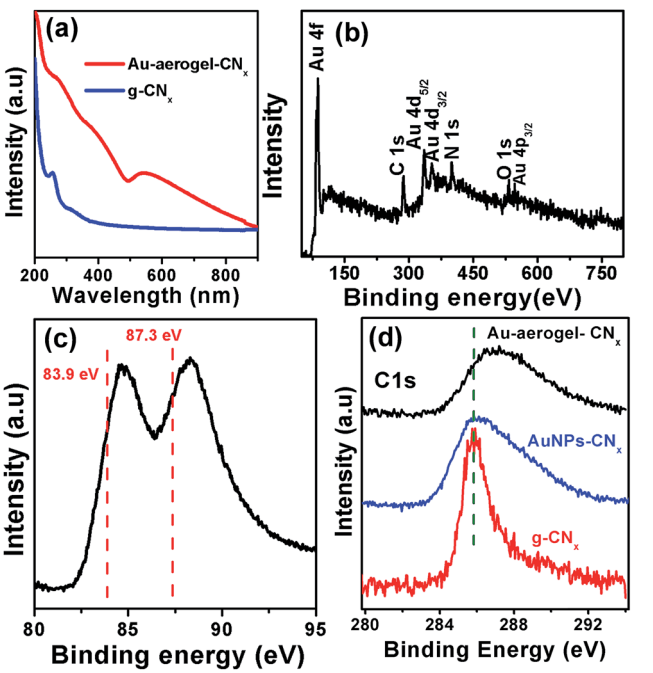

Fig. 4 (a) UV-visible spectra of g-CN_x and Au–aerogel–CN_x. (b) XPS survey scan of Au–aerogel–CN_x. XPS spectra of (c) Au 4f orbital and (d) C1s for Au–aerogel–CN_x (black line), AuNPs–CN_x (blue line), and g-CN_x (red line).

(XPS) and FT-IR spectroscopy were used to examine the change in the electronic structure of the CN_x framework in the presence of AuNPs and Au–aerogels. The FT-IR spectra of g-CN_x in Fig. S3 (ESI†) show two peaks at 1230 cm^{-1} and 1400 cm^{-1}, which can be attributed to aromatic C=N stretching and the peak at 1600 cm^{-1} can be assigned as C=N stretching. These three peaks disappeared and a new intense peak at 1380 cm^{-1} appeared when AuNPs were dispersed into the CN_x matrix. The FT-IR spectrum of the Au–aerogel–CN_x compound is also completely different from those of the free CN_x and AuNPs–CN_x compounds. The peaks at 1116 and 1024 cm^{-1} can be attributed to the C–N single bond and the peak at 1636 cm^{-1} is attributed to the C=N double bond. The aqueous solutions of AuNPs–CN_x and Au–aerogel–CN_x compounds were evaporated separately and the solid products were used for FT-IR measurements. However, FT-IR spectra of the freshly prepared powder sample were also taken. The IR spectra of the freshly prepared AuNPs–CN_x powder are similar to those of the free CN_x compound whereas the spectra of freshly prepared Au–aerogel–CN_x are completely different from those of the free CN_x compound (Fig. S3, S4a and b, ESI†). This indicates that the Au aerogel is chemically attached to CN_x sheets and AuNPs are physically adsorbed in the freshly prepared AuNPs–CN_x powder sample. Fig. 4b shows the survey scan of the XPS spectrum which clearly indicates the presence of gold, carbon, nitrogen and oxygen atoms in the AuNPs–CN_x composite. It is well known that the binding energy spectra of Au 4f of metallic AuNPs appear as a doublet with a binding energy of 83.9 eV for $4f_{7/2}$ and 87.3 for $4f_{5/2}$ peaks.[55] Fig. 4c displays the Au 4f spectrum for Au–aerogel–CN_x which shows two peaks at 84.7 and 88.4 eV. The peaks at 84.7 and 88.4 eV can be assigned to Au $4f_{7/2}$ and $4f_{5/2}$ photoelectrons. This binding energy shift suggests the strong interaction between the Au aerogel and CN_x support. The carbon 1s (C1s) and nitrogen 1s (N1s) XPS spectra of CN_x were deconvoluted to three and two main Gaussian peaks, respectively (Fig. S5a and b†). The peaks at 285.45 (C1) and 286.35 eV (C2) were assigned to the presence of (sp^2) [N–C]N(sp^2) (carbon bonded to two nitrogen atoms) and C(–N)$_3$ (planar trigonal carbon geometry), respectively, whereas the peaks at 400.3 and 401.4 eV suggest the presence of (sp^2) C–N(sp^2) or a pyridine moiety and quaternary nitrogen, respectively. The comparison of C1s and N1s XPS spectra of CN_x, AuNPs–CN_x and Au–aerogel–CN_x is shown in Fig. 4d and S5c (ESI†), respectively. This shows that the positions as well as the shapes of the C1s XPS spectra of CN_x in the presence of Au–aerogel–CN_x are significantly different from those of free CN_x. The C1s peaks become broad and a shift of 1.6 eV towards higher binding energy was observed when the Au–aerogel is supported on the CN_x framework, but the positions of N1s peaks remain unaffected. Therefore, the change in the binding energy of carbon and Au confirms that there is strong interaction between carbon and Au in the Au–aerogel–CN_x composite. As shown in Fig. S5c (ESI†) the binding energy of 1s nitrogen in AuNPs–CN_x is 1 eV higher than that of free CN_x whereas the position of C binding energy is almost the same and only broadening of the peak is observed (Fig. 4d). Thus, it can be concluded that nucleation of Au nanoparticles occurs at the carbon site in the case of Au–aerogel–CN_x whereas nucleation occurs at the nitrogen site for AuNPs–CN_x.

Based on TEM, SEM, XPS, and FT-IR spectroscopic studies, the formation mechanism of the Au metal aerogel supported on CN_x sheets was proposed (Scheme 1). Since during the synthesis of the Au–aerogel–CN_x composite, a large number of Au atoms are produced in a very short time due to the fast reduction of $HAuCl_4$ by $NaBH_4$, nucleation of AuNPs takes place at the carbon centre in CN_x sheets and finally growth takes place to form Au–aerogel on CN_x sheets. However when no $NaBH_4$ is used, reduction of $HAuCl_4$ due to ultrasonication produces gold atoms at a slow rate, and gold particles are physically adsorbed on the surface of CN_x sheets leading to precipitation of the AuNPs–CN_x composite. On evaporation of aqueous solution of the AuNPs–CN_x composite on a solid substrate, first 2D sheets

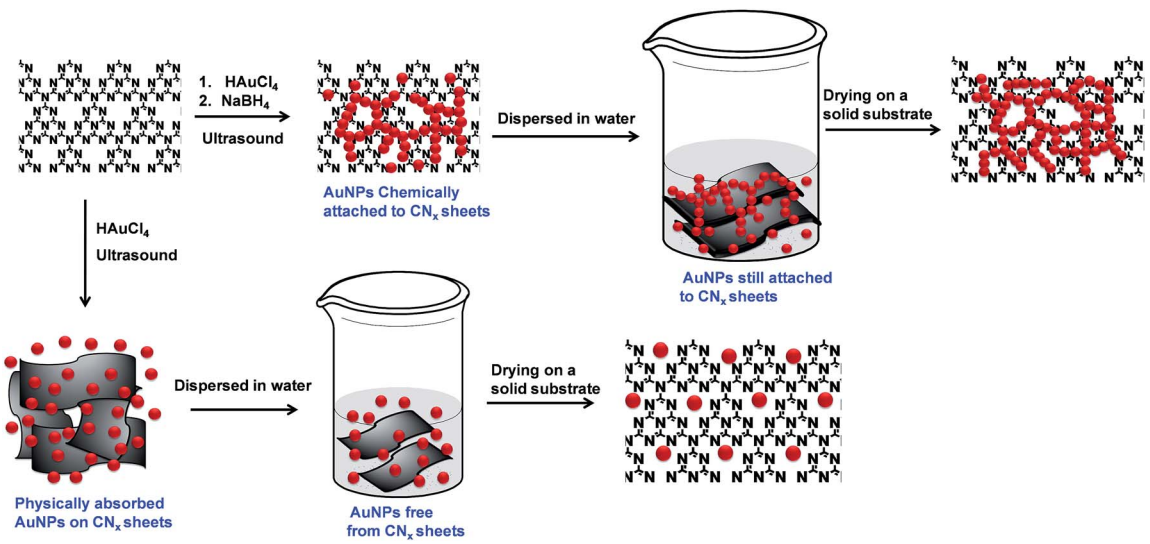

Scheme 1 Schematic representations of the formation of Au–aerogel and AuNPs on the CN_x sheet.

of CN_x are formed followed by nucleation at the nitrogen atom, after which growth occurs to form an assembly of gold nanoparticles on CN_x sheets.[26] Formation and evaporation induced ordered assembly of silver nanoparticles on CN_x sheets was also reported by our group recently.[30]

Electrochemical characterization

The electrochemical activity of the freshly prepared Au–aerogel–CN_x composite modified GC electrode was first investigated using cyclic voltammetry (CV) with the $Fe(CN)_6^{3-/4-}$ redox couple. Fig. 5a represents the CVs of the GC electrode and Au–aerogel–CN_x as well as AuNPs–CN_x modified GC electrode recorded in 0.05 M H_2SO_4 solution containing 0.5 mM $K_4[Fe(CN)_6]$. This shows the significant improvement of the catalytic activity at the Au–aerogel–CN_x/GC electrode in comparison to bare GC. It is well known that the electrochemical reaction of $[Fe(CN)_6]^{3-/4-}$ is sensitive to surface microstructure and surface chemistry, but has a less significant effect on oxygen functionalities in a carbon based electrode.[56,57] The CV at the GC electrode showed a redox peak with a peak potential difference (ΔE_p) of 75 mV indicating a quasi-reversible redox reaction. For the Au–aerogel–CN_x modified GC electrode, both anodic and cathodic current densities increased significantly and 13 mV decrease of ΔE_p was observed in comparison to the bare GC electrode. The observed ΔE_p values at Au–aerogel–CN_x–GC and AuNPs–CN_x/GC are 62 mV and 66 mV, respectively. The decrease of the ΔE_p value with enhancement of peak currents at Au–aerogel–CN_x–GC suggests facile fast electron-transfer kinetics for this redox couple. As shown in Fig. S6 (ESI†), both the oxidation and reduction peaks of currents at the three Au–aerogel–CN_x/GC, AuNPs–CN_x/GC and GC electrodes increased linearly with the square root of the scan rate, indicating that the reaction is controlled by a semi-infinite linear diffusion. The larger slope values of the linear regression equation (Table T1, ESI†) and low ΔE_p suggest that[57] the unique electron structure and requisite surface structure endow Au–aerogel–CN_x film with fast electron and mass transfer.

Voltammetry method was used for further electrochemical characterization of the synthesized composite. CV was carried out in both 0.5 M H_2SO_4 and 0.5 M KOH media in a N_2 saturated atmosphere. Representative voltammograms are shown in Fig. 5b and c. In acidic solution the anodic peak at $E > 1.4$ V can be attributed to the formation of Au surface oxides and the cathodic peak at 1.1 V to the reduction of these surface oxides.[58] The large background arises mainly due to the high surface area of the Au–aerogel on the CN_x support. In an alkaline (KOH) medium Au surface oxidation and reduction are also visible. Au oxidation peak is observed at $E > 1.2$ V and reduction peak at 1.0 V. The real electrochemical surface area (ECSA) of the samples was determined by using cyclic voltammograms by using charge integration of the reduction peak of gold oxide and the reduction value of the monolayer was assumed to be 400 μC cm^{-2}. From CV it is evident that ECSA increases as the porous network structure is formed. The ECSA values of AuNPs–CN_x, commercial flat Au electrode, Au–aerogel(1)–CN_x, and Au–aerogel(2)–CN_x are 0.14, 0.17, 1.17 and 1.05 per cm^2 (Table T2, ESI†) in acidic medium. The surface areas of porous Au–aerogel–CN_x samples are much higher than those of AuNPs–CN_x and commercial flat Au electrode. In alkaline medium also Au–aerogel–CN_x has a higher ECSA value than AuNPs–CN_x and commercial flat Au electrode (Table T2, ESI†).

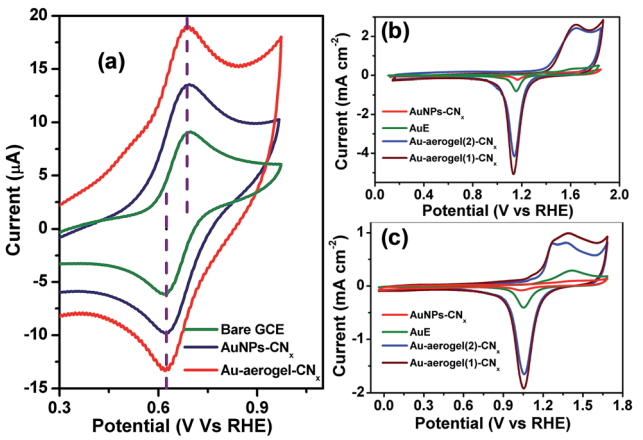

Fig. 5 (a) CVs of 0.5 mM $Fe(CN)_6^{3-/4-}$ solution at GCE, AuNPs–CN_x and Au–aerogel–CN_x modified GC electrode. Electrolyte: 0.05 M H_2SO_4 solution. (b) CVs of AuNPs–CN_x, commercial flat Au electrode, Au–aerogel(1)–CN_x, Au–aerogel(2)–CN_x in N_2 saturated 0.5 M H_2SO_4 solution and (c) CVs of AuNPs–CN_x, commercial flat Au electrode, Au–aerogel(1)–CN_x, Au–aerogel(2)–CN_x in N_2 saturated 0.5 M KOH solution. Scan rate 100 mV sec^{-1}.

ORR studies on Au–aerogel–CN_x catalysts in alkaline medium

The electrochemical behaviour of Au–aerogel–CN_x samples was investigated towards oxygen reduction reaction (ORR). ORR is a complex multielectron reaction that involves different elementary steps with different intermediates.[59] Oxygen can be electrochemically reduced either directly to water (direct 4e reduction) or through the formation of H_2O_2 (2e reduction) and then this peroxide can be reduced to water (series 2e reduction) or chemically decomposed on the electrode or desorbed in bulk. Production of H_2O_2 in fuel cells is not desirable as it can corrode the membrane electrode assembly. Therefore, much effort has been made for the preparation of Pt, Pd, and Au based catalysts to decrease the overpotential and H_2O_2 formation. To examine the catalyst activity we performed the ORR in alkaline medium. Fig. 6a shows the typical linear sweep voltammetric (LSV) curves for ORR at CN_x, AuNPs–CN_x, porous-Au–aerogel(1)–CN_x and Au–aerogel(2)–CN_x modified GC electrodes in O_2 saturated 0.5 M KOH medium with a Au loading of 0.130 mg cm^{-2} each. All the modified electrodes show a LSV peak in O_2 saturated KOH solution and the Au–aerogel–CN_x modified electrode does not show any peak in nitrogen saturated KOH medium suggesting the ORR activity of these electrodes. The CN_x modified GC shows a weak peak at 0.48 V (*vs.* RHE). When the GC electrode was modified with AuNPs–CN_x and Au–aerogel–CN_x, a stronger peak appeared at 0.61 V and 0.8 V respectively. The porous-Au–aerogel(1)–CN_x and porous-Au–aerogel(2)–CN_x modified GC electrode showed better ORR activity than the AuNPs–CN_x electrode, with a much stronger cathodic peak and more

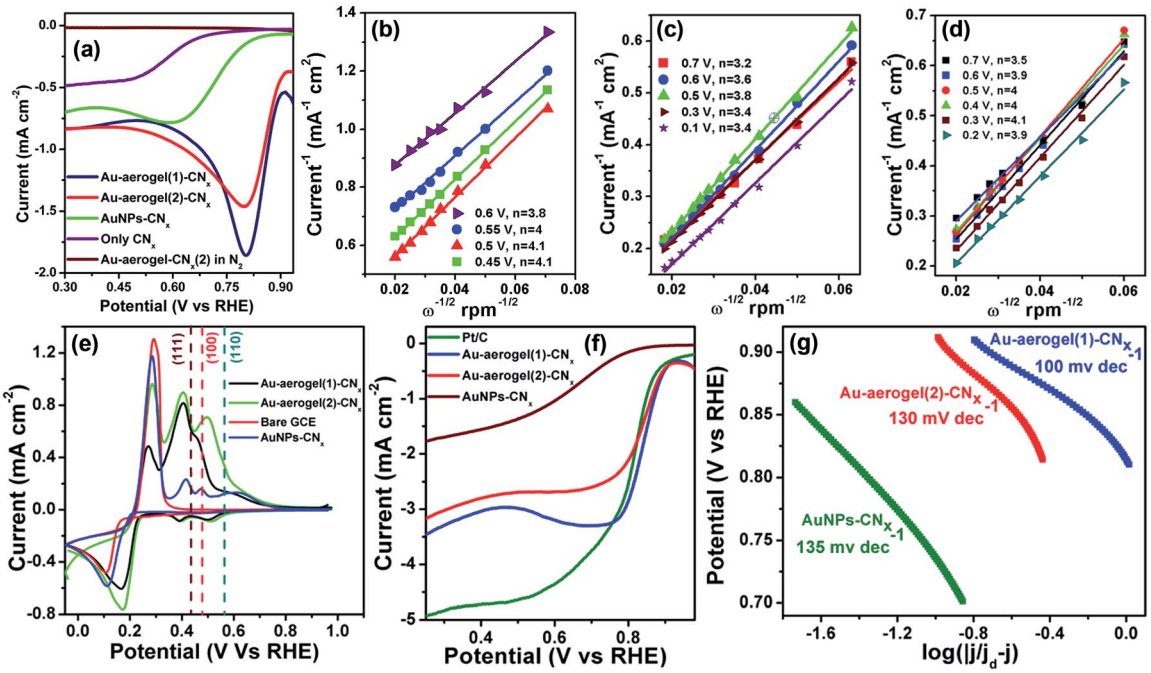

Fig. 6 ORR performance by various electrodes: (a) LSV curves at Au–aerogel(1)–CN_x/GCE, Au–aerogel(2)–CN_x, and AuNPs–CN_x, CN_x modified GC electrode in the presence of oxygen saturated KOH medium and Au–aerogel(2)–CN_x in the presence of nitrogen saturated solution. (b–d) K–L plot of the ORR of AuNPs–CN_x/GCE, Au–aerogel(1)–CN_x/GCE, and Au–aerogel(2)–CN_x/GCE. (e) Voltammetric profile of Au–aerogel–CN_x, AuNPs–CN_x and GCE in 0.1 M KOH solution containing 2 mM $Pb(NO_3)_2$ solution at a scan rate of 10 mV sec^{-1}. The main Pb desorption peaks from Au surfaces are marked. (f) Comparison of LSV polarization curves of Au–aerogel–CN_x and Pt/C-GCE at 1000 rpm rotation speed. (g) The mass transfer corrected Tafel slope of different catalysts is shown. All ORR experiments were conducted in oxygen saturated 0.5 M KOH solution at a scan speed of 100 mV sec^{-1}. Au loading: 0.130 mg cm^{-2}.

positive onset potential at ~0.92 V with $E_{1/2}$ of ~0.855 V. This suggests that the porous Au–aerogel–CN_x can reduce oxygen more easily than AuNPs–CN_x.

The kinetics of ORR at the modified electrode was studied using a rotating disk electrode (RDE) in oxygen saturated 0.5 M KOH solution. Fig. S7a (ESI†) shows the LSV polarisation (current density *vs.* applied potential) curve for ORR on the AuNPs–CN_x electrode at different rotation speeds varying from 200 rpm to 2500 rpm. From the figure it is obvious that current density increases with increasing rotation speed. The number of electrons involved per O_2 in ORR can be determined from the Koutecky–Levich (K–L) equation (for detailed information see the ESI†). Fig. 6b shows the K–L plot of ORR on the AuNPs–CN_x electrode at different voltages, ranging from 0.45 to 0.6 V constructed from Fig. S7a.† The linearity of the K–L plots and their near parallelism suggest first order reaction kinetics with respect to the concentration of dissolved oxygen. At the foot of the polarization curve (0.6 Volt) the *n* value is little lower than 4 (3.8) and it is 4 at 0.55 V or a less positive voltage. From the K–L plot it can be concluded that mainly a 4e transfer ORR process predominates over the AuNPs–CN_x surface. However, a very small amount of 2e process also occurs at the foot of the polarization curve. Fig. S7b and c (ESI†) show LSV polarisation curves for ORR on Au–aerogel(1)–CN_x and Au–aerogel(2)–CN_x modified electrodes at different rotation speeds. The corresponding K–L plots constructed from Fig. S7b and c (ESI†) are shown in Fig. 6c and d, respectively. The *n* value is 3.5 at 0.7 V for the Au–aerogel(2)–CN_x electrode which increases with decreasing voltage and reaches 4 at 0.6 V (Fig. 6d). Similar 4e reduction and some 2e along with the 4e reduction process at the foot of the curve are also observed for the Au–aerogel(1)–CN_x electrode (Fig. 6c). Thus, these results indicate that gold–carbon nitride hybrids favour a 4e oxygen reduction process. It is known that the reduction of oxygen at the gold surface can occur *via* either a 2e pathway producing hydrogen peroxide or 4e pathway forming water.[58]

It has also been reported that the surface structure of the gold nanoparticles can influence their electrochemical ORR behaviour.[60,61] The 4e reduction mechanism takes place on the Au(100) crystal surface whereas the 2e reduction of oxygen occurs on Au(111) and Au(110) crystal surfaces. In addition, it has also been reported[62] that ORR activity at these crystal planes decreases in the order Au(100) > Au(110) > Au(111). The presence of a surface modifier during the synthesis of gold nanoparticles can influence the formation of a specific surface structure. For example, the (100) or (111) facet of gold was formed if gold nanoparticles were synthesized in the presence of iodide whereas sulphide induces the formation of the (110) facet of gold.[60] The highest catalytic activity and 4e reduction of oxygen was reported by Hernández *et al.*[60] when gold nanoparticles were synthesized in water-in-oil microemulsion in the presence of iodide. Gold nanoparticles, dispersed in the conducting polymer-poly(aminothiophenol), exhibited 4e reduction of oxygen due to the presence of the poly(aminothiophenol)

surface modifier.[63] H. Erikson[58,64] reported that at a low potential H_2O_2 (2e) predominates and at a more negative potential H_2O_2 is further reduced (4e) to water. Tokeo Ohsaka *et al.*[65] also reported 4e reduction of oxygen to water on crystallographically oriented Au(100)-like gold nanoparticles at a reasonably low cathodic overpotential. In the case of AuNPs–CN_x, Au–aerogel(1)–CN_x, and Au–aerogel(2)–CN_x the n value reaches 4 at a small overpotential. So it can be concluded that OH^- formation is the major pathway rather than OH_2^- formation. In order to get an insight into Au surface structure in Au–aerogel–CN_x composites, a Pb adsorption–desorption experiment was performed in 2 mM $Pb(NO_3)_2$ dissolved in 0.1 M KOH solution (Fig. 6e). The peak potential recorded signifies the orientation of Au surfaces. The main Pb desorption peak for Au(111), (100) and (110) facets generally arises at 0.435, 0.475 and 0.56 V, respectively. Fig. 6e represents the complete lead underpotential deposition (UPD) curve for the AuNPs–CN_x modified GC electrode. The strong peaks at 0.435 and 0.475 V suggest that the Au(111) and (100) facets predominate in Au–aerogel–CN_x with a slightly lower surface area of Au(110) facets. Since the ORR activity of the Au(100) facet is much higher than that of the Au(110) facet, a small portion of the Au(100) crystalline plane is sufficient to induce the 4e reduction of oxygen. It can be concluded that since the synthesis of the Au–aerogel was performed in the presence of CN_x sheets, CN_x acts as a surface modifier to form the electrochemically active Au(100) crystal plane in the Au–aerogel–CN_x composite; oxygen reduction at the AuNPs–CN_x composite surface thus probably occurs *via* the 4e reduction pathway to form water. At low potentials H_2O_2 (2e) predominates and at more negative potentials H_2O_2 is further reduced (4e) to water. The comparison of the ORR activity at the Au aerogel–CN_x catalyst with that at the Pt/C catalyst is presented in Fig. 6f. This shows that the half-wave potential ($E_{1/2}$) for O_2 reduction on Au–aerogel–CN_x is more positive than the commercial Pt/C catalyst. $E_{1/2}$ on Au–aerogel–CN_x is 30 mV more positive than that of Pt/C. The $E_{1/2}$ value for AuNPs–CN_x was found to be lower than that of Au–aerogel–CN_x. The superior ORR activity at Au–aerogel–CN_x to that of other catalysts can be explained by the high electrochemical surface area of this catalyst (Table 1). The ECSA of AuNPs–CN_x was small and thus $E_{1/2}$ was less positive. As $E_{1/2}$ does not represent the intrinsic property of the catalysts, the SA and MA values calculated at 0.6 V (RHE) are also given in Table 1 (for detailed information see the ESI†). The SA values for porous Au–aerogel–CN_x catalysts are higher than those of AuNPs–CN_x. The considerably lower SA value for small AuNPs (2 nm) is due to the particle size effect[39] and particularly the crystallographic orientation of AuNPs.[58] It has been reported recently that the ORR activity of AuNPs is negative when the particle size is ~2 nm,[36] but when the particle size was 17–40 nm,[37] the ORR activity becomes comparable with that of bulk gold. So from the above observations it can be concluded that the larger particle size in the porous network structure of Au–aerogel supported on CN_x is responsible for the higher catalytic activity. The MA values for porous Au–aerogel(1)–CN_x are slightly higher than those of Au–aerogel(2)–CN_x and much higher than those of the AuNPs–CN_x catalyst. Mass transport corrected Tafel slope values for oxygen reduction over bulk gold and platinum have been reported to be close to −120 mV dec^{-1}. The Tafel slopes for Pt based[66,67] catalysts lie between 60 and 70 mV dec^{-1} (at low overpotentials) and increase up to ~120 mV dec^{-1} with increasing overpotential. This low Tafel slope (60–70 mV dec^{-1}) arises due to the formation of clogged oxide species at the surface active sites. The Tafel plots were obtained after the measured currents were corrected for diffusion to provide the kinetic currents in the mixed activation–diffusion region, calculated from the equation

$$J_k = jj_d/(j_d - j)$$

where $j/(j_d - j)$ is the mass transfer correction term.

The mass transport correction was made using the limiting current

$$j_d = B\omega^{1/2}$$

where ω is the rotation rate (rpm) of the electrode.

Mass transfer corrected Tafel plots, constructed from RDE analysis for ORR activities are shown in Fig. 6g. The Tafel slope for the Au–aerogel(1)–CN_x sample is ~100 mV dec^{-1} whereas for the other two compounds the slopes are 130 and 135 mV dec^{-1}. In all three Au–CN_x composites the Tafel slope lies between 100 and 140 mV dec^{-1} which is close to that of bulk Au (120 mV dec^{-1}) and some Au based catalysts reported in the literature .[64] This suggests that the transfer of the first electron is the rate determining step for O_2 reduction on gold surface in alkaline medium. A large Tafel slope of ~160 mV dec^{-1} as well as a small slope of ~60 mV dec^{-1} were reported by various groups[58,64] in the literature for the Au/C ORR catalyst. Table 2 lists some Au based catalytic activities previously reported in the literature. This catalyst has a comparable activity to and in some case better catalytic activity in terms of the onset potential and half wave potential ($E_{1/2}$) than those reported in the literature.

To evaluate the properties of a catalyst, methanol crossover effect should be evaluated carefully as fuel molecules (methanol, glucose) from the anode sometimes permeate to the cathode and seriously affect the activity of the cathode material.[34,68] Crossover effect is one of the prime problems in

Table 1 Different parameters of the synthesized catalysts at 0.5 M KOH

Catalyst	A_r	$E_{1/2}$	SA at 0.6 V (mA cm^{-2})	MA at 0.6 V (Ag^{-1})	Tafel slope (mV dec^{-1})
AuNPs–CN_x	0.07	+0.6	1.42	12	135
Au–aerogel(1)–CN_x	0.6	+0.854	2.91	190	100
Au–aerogel(2)–CN_x	0.5	+0.860	2.12	115	130

Table 2 Comparison of the ORR activity of different catalysts in acidic and alkaline media

Catalyst	Medium	$E_{1/2}$ (V) (*vs.* RHE)	Tafel slope (mV dec^{-1})	Ref.
5 nm Au spheres	Alkaline	0.78	43	58
30% Au/C	Alkaline	0.725	114	64
Fe_x N-NGA	Alkaline	~0.860	59	70
Au@rGO	Alkaline	~0.763	—	71
C−$Mn_xFe_{3-x}O_4$ NPs	Alkaline	~0.809	—	72
30% Au/C	Acidic	0.218	181	64
5 nm Au spheres	Acidic	0.238	139	58
2 nm Au thin film	Acidic	—	109	69
PtNi–CN_1	Acidic	0.8	120	66
Pt-dendrimer	Acidic	0.9	—	73
Au–aerogel–CN_x	Acidic	0.33	~155	This work
Au–aerogel–CN_x	Alkaline	0.860	~130	This work

methanol fuel cells for the Pt/C catalyst. Fig. S8(a and b, ESI†) shows the cyclic voltammograms of the Pt/C and Au–aerogel–CN_x electrodes in oxygen saturated 0.5 M KOH in the presence of 2 M methanol. Pt–C shows a very strong methanol oxidation peak (0.83 V) and very weak oxygen reduction peak (0.810 V) but no noticeable response for methanol oxidation was observed in our Au–aerogel–CN_x catalyst under the same experimental conditions. In both cases no peak was observed in a N_2 atmosphere. So we conclude that our catalyst has high selectivity towards ORR and possesses a good tolerance to the cross-over effect of methanol. Besides the high catalytic activity, Au–aerogel–CN_x also exhibits considerable stability. In alkaline medium the catalyst was stable up to 25 000 seconds with 65% retention of chronoamperometric current. The stability of Au–aerogel–CN_x is slightly better than that of Pt/C whereas the stabilities of AuNPs–CN_x and Pt/C are comparable. Thus Au–aerogel–CN_x is superior to the commercial Pt–C catalyst in terms of ORR peak position, stability and methanol tolerance.

ORR studies on Au–aerogel–CN_x catalysts in acidic medium

The catalytic activity of Au–aerogel–CN_x was further evaluated by ORR in acidic medium. As reported, in acidic medium Au possesses modest catalytic activity, but its catalytic activity is considerably higher than that of carbon materials. We investigated the catalytic activity of the porous Au–aerogel to show the versatility of our catalysts. CV and LSV techniques were used to evaluate the catalytic efficiency of Au–aerogel–CN_x. Fig. 7a shows the LSV curves of the commercial flat Au electrode, AuNPs–CN_x, Au–aerogel(2)–CN_x, and Au–aerogel(1)–CN_x modified GC electrodes in 0.5 M H_2SO_4 with a catalyst loading of 0.130 mg cm^{-2} each. For comparison the ORR activity of commercial 10% Pt/C is shown. The commercial flat-Au electrode shows ORR activity with a cathodic peak at −0.05 V and an onset potential of +0.20 V. The Au–aerogel–CN_x composites are the most active ORR catalysts with much stronger cathodic peaks and more positive onset potentials. The cathodic peaks were observed at +0.22 V (*vs.* RHE) for Au–aerogel(2)–CN_x and Au–aerogel(1)–CN_x modified electrode with onset potentials of 0.6 V and 0.43 V (RHE) respectively. The complete CV scan for

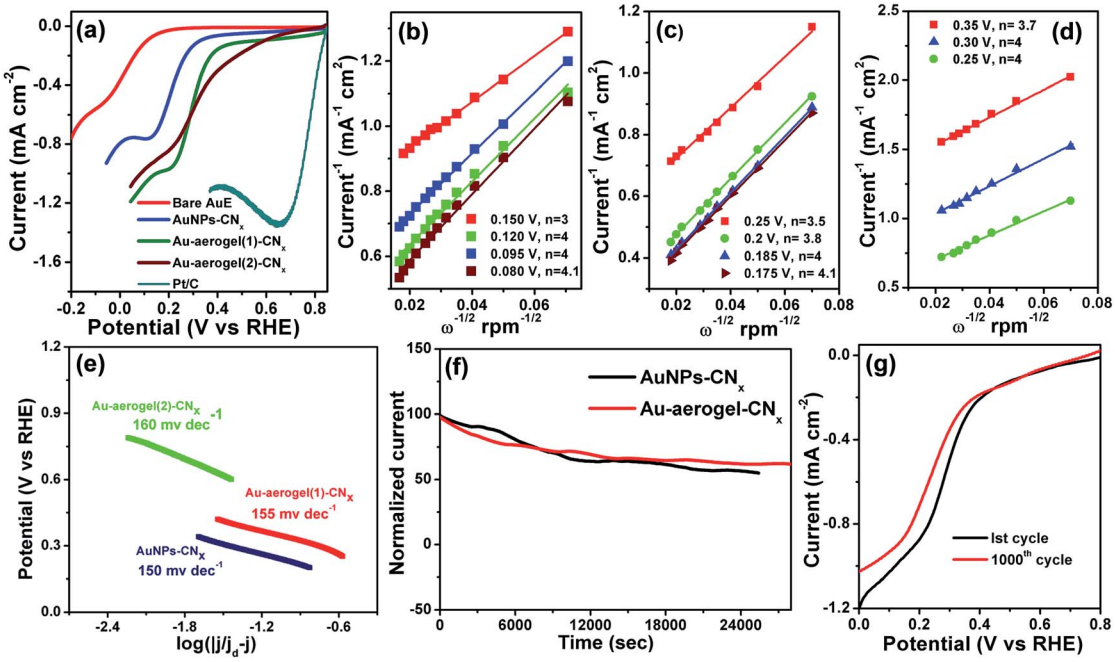

Fig. 7 ORR performance by various electrodes in acidic medium: (a) LSV curves for AuNPs–CN_x, Au–aerogel(1)–CN_x, Au–aerogel(2)–CN_x, and flat AuE in oxygen saturated 0.5 M H_2SO_4 solution. (b, c, and d) K–L plots of the ORR for AuNPs–CN_x/GCE, Au–aerogel(1)–CN_x/GCE, and Au–aerogel(2)–CN_x/GCE constructed from the polarisation curves. (e) Mass corrected Tafel slopes of different catalysts are shown. (f) Chronoamperometric responses of Au–aerogel–CN_x and AuNPs–CN_x at 0.15 V. (g) Stability of the catalyst up to the 10 000th cycle. All ORR experiments were conducted in oxygen saturated 0.5 M H_2SO_4 solution at a scan speed of 100 mV sec^{-1}. Au loading: 0.130 mg cm^{-2}.

these catalysts in O_2 saturated KOH medium is given in Fig. S9 (ESI†). The ORR performance of the AuNPs–CN_x catalyst is better than that of the flat Au electrode but inferior to that of the Au–aerogel–CN_x electrode.

The RDE method was also used to study the kinetics of oxygen reduction in O_2 saturated 0.5 M H_2SO_4 solution. Fig. S10a† shows LSV polarization curves (current density–potential curves) of ORR for the AuNPs–CN_x electrode at different rotation speeds. The corresponding K–L plot for the AuNPs–CN_x electrode is shown in Fig. 7b. As shown in Fig. 7b, the linearity of the plot and parallelism of fitting curves suggest first order kinetics with respect to the concentration of O_2. The value of n at 0.15 V (foot of the polarization curves) was ~3 and it increased to 4 at 0.12 V. This suggests that although some 2e transfer process occurs at low overpotentials, ORR is mainly dominated by the 4 electron transfer process where O_2 is directly reduced to OH^-. The LSV polarization curves of Au–aerogel(1)–CN_x and Au–aerogel(2)–CN_x modified electrodes are shown in Fig. S10, b and c†, respectively. The corresponding K–L plots are given in Fig. 8c and d. As in the previous case, ORR at Au–aerogel–CN_x electrodes in acidic medium is mainly guided by a direct 4 electron reduction mechanism.

Mass transfer corrected Tafel slopes (Fig. 7e) were found to be 160 mV dec^{-1}, 155 mV dec^{-1} and 150 mV dec^{-1} for Au–aerogel(2)–CN_x, Au–aerogel(1)–CN_x, and AuNPs–CN_x which are slightly higher than the typical value of 120 mV dec^{-1} reported for bulk Au previously.[64,69] The similar high value of the Tafel slope in acidic medium was also reported for carbon supported gold nanoparticle based catalysts.[58] Moreover the catalysts were highly stable in acidic medium. A chronoamperometric measurement (Fig. 8f) was carried out at a fixed potential of 0.15 V (RHE) which showed that 60% current was retained after 20 000 s. From Fig. 7g it is also evident that the current density decreased slightly after 10 000 LSV scans. So our Au–aerogel–CN_x catalyst shows sufficient stability in acidic medium also. A comparison of different Au composite catalysts used in this work towards ORR is presented in Table T3 (ESI†). From Fig. 7a and Table T3† it may be concluded that the ORR

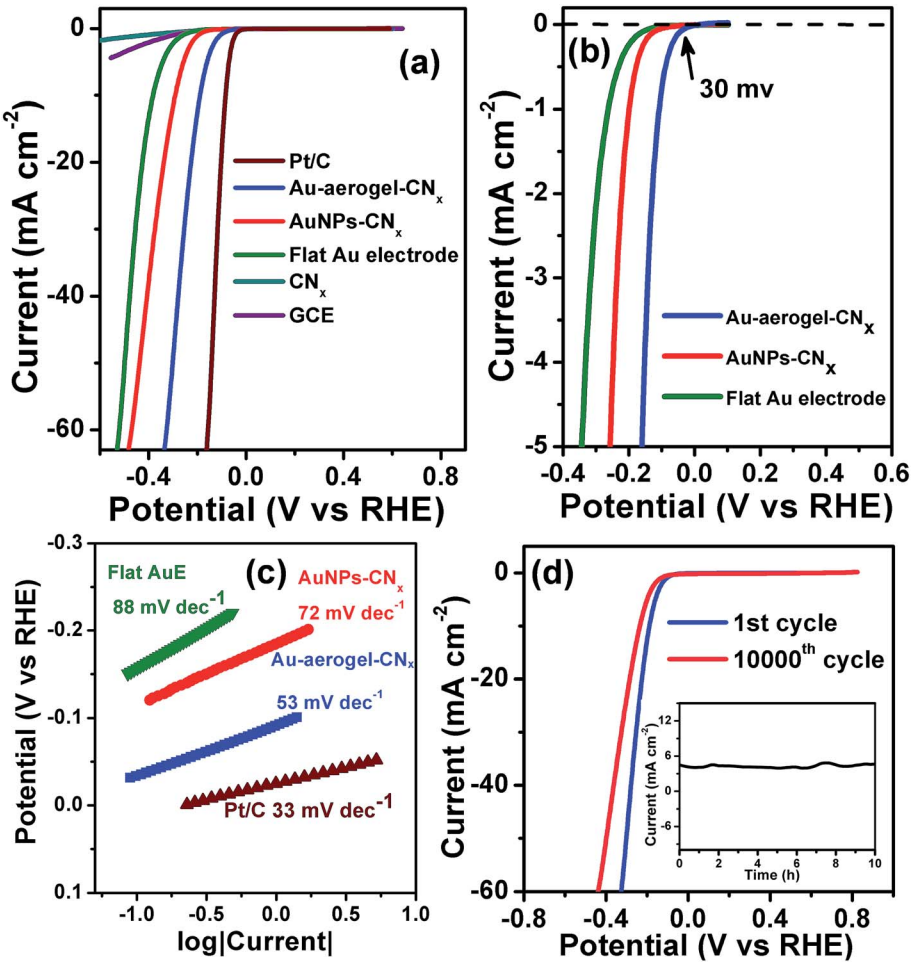

Fig. 8 HER performance by various electrodes: (a) LSV polarisation curves of Pt/C, Au–aerogel–CN_x, AuNPs–CN_x, Au electrode, CN_x, and GCE in N_2 saturated 0.5 M H_2SO_4 solution (scan rate 10 mV sec^{-1}, rotation speed 1000 rpm). (b) Base line corrected LSV polarisation curves of Au–aerogel–CN_x, AuNPs–CN_x, and Au electrode. (c) HER Tafel plots (log j *vs.* potential) of Pt/C, Au–aerogel–CN_x–GCE, AuNPs–CN_x, and Au electrode. (d) HER activity of the Au–aerogel–CN_x electrode in the 1st cycle and after 10 000 scans (at a scan speed of 50 mv sec^{-1}). Inset: chronoamperometric responses of Au–aerogel–CN_x for a long period of time (10 h) at −0.15 V (RHE). Au loading: 0.130 mg cm^{-2}.

activity of these Au composites in acidic media depends on the morphology of the catalysts. The onset potentials for oxygen reduction in acidic medium at the commercial flat Au electrode, 2 nm AuNPs supported CN_x, and Au–aerogel supported CN_x modified GC electrodes are found to be 0.20 V, 0.37 V and 0.6 V, respectively, and $E_{1/2}$ values are found to be 0.03 V, 0.21 V and 0.33 V, respectively. This suggests that the ORR activity on the Au–aerogel–CN_x electrode is the highest and that on the commercial flat Au electrode is the poorest. The high electrochemical surface area of the Au–aerogel–CN_x catalyst is due to its porous interconnected network and crystallographic orientation of bigger Au particles. This porous structure also helps in easy mass transport of the reactant or product to catalytically active sites. For better comparison SA and MA (at 0.25 volt *vs.* RHE) are also given in Table T3 (ESI†). The SA values of AuNPs–CN_x and Au–aerogel–CN_x are the same, but the MA value changes for different catalyst morphologies. Table 2 lists some data for catalytic activities in alkaline and acidic media reported in the literature. The Au–aerogel–CN_x catalyst has a comparable ORR activity to or better activity than the Pt/C catalyst in basic media and its activity in acidic media is better than that of any previously reported Au based catalyst. The high electrochemical surface area of Au–aerogel–CN_x is probably not the only reason for its superior ORR performance. It has been reported recently that AuNPs less than 2 nm act as a negative electrocatalyst for oxygen reduction. The ORR activity in acidic medium at the citrate capped 2 nm AuNPs modified GC electrode is better than that of bare GC, but much inferior to that at the bare gold electrode. But the present work reports much better performance for 2 nm AuNPs, supported on CN_x sheets towards oxygen reduction than that of the bare gold electrode in acidic medium (Fig. 7a and S9, ESI†). Thus this shows that the CN_x support plays an important role in making the 2 nm AuNPs a strong positive electrocatalyst. A shift of C1s or N1s peaks and Au 4f peaks in the XPS spectra of Au composites was observed, suggesting that the gold nanoparticles are directly bonded to the CN_x sheets. FT-IR spectra of these also confirm that the change in the electronic structure of CN_x sheets is due to the presence of nanoparticles of Au on CN_x sheets. The strong interaction and the transfer of electrons between them lead to change in the electronic state of gold and CN_x sheets. The CV studies of $K_4[Fe(CN)_6]$ at the modified GC electrode also confirm a more facile electron transfer at the porous Au–aerogel–CN_x electrode. In addition several groups[22,74] reported that the catalytic activities of supported gold nanoparticles are due to the extra negative charge at the periphery of the gold nanoparticles resulting from the interaction between the nanoparticles and support. It has been reported that charged gold nanoparticles on a MgO support[22] promote the activation of adsorbed reactant molecules such as O_2. It has also been reported[75] that the tolerance of nanoparticle loaded C_3N_4 electrocatalysts increases with increasing concentration of nitrogen on the C_3N_4 support. The conductivity of the support increases and the electrochemical behaviour becomes closer to that of the Pt/C catalyst when a low nitrogen concentration is present in the C_3N_4 support. Recently, V. Di Noto and his co-workers reported[75,76] the relationship between nitrogen concentration, structure morphology, and electrochemical ORR performances of PdCoNi "core–shell" C_3N_4 electrocatalysts. When the concentration of N in the carbon nitride shell is low and the cell constant of PdCoNi alloy NPs is lowest, the best ORR activities were observed.[75] Various groups reported[77,78] that heteroatoms such as nitrogen based ligands can easily coordinate metal nanoparticles and hence the metal–support interaction improves the tolerance as well as the activity of the electrocatalysts under oxidation conditions. Similar behaviour was also observed in the case of the Au–aerogel–CN_x composite. The concentration of N is lower in Au–aerogel–CN_x than in AuNPs–CN_x and better activity on Au–aerogel–CN_x was observed. Although the same support (CN_x) was used for AuNPs–CN_x and Au–aerogel–CN_x catalysts, the nature of interaction between CN_x and gold is distinctly different as suggested by FT-IR and XPS studies. This suggests that the CN_x support (AuNPs–CN_x interaction) plays an important role in the enhancement of the ORR activity at the porous Au–aerogel–CN_x composite. In addition, the porous morphology of gold in Au–aerogel–CN_x may help in the adsorption of reactants such as O_2 and desorption of products from the electrode surface facilitating oxygen reduction. Therefore, we may conclude that the unique synergistic effects of CN_x and Au–aerogel–CN_x, due to the strong interaction between CN_x and porous Au/AuNPs make the porous Au–aerogel–CN_x composite a superior electrocatalyst for oxygen reduction.

HER studies on the Au–aerogel–CN_x catalyst in acidic medium

The catalytic activity of AuNPs–CN_x and Au–aerogel–CN_x catalysts was then investigated for the HER process. The HER activity was studied in 0.5 M H_2SO_4 solution in a nitrogen saturated system using three electrode linear sweep voltammograms at a scan speed of 10 mV sec^{-1}. The representative linear sweep voltammogram curves of geometric current density (mA cm^{-2}) *vs.* applied potential show HER activities of bare GCE, CN_x, commercial flat AuE, AuNPs–CN_x, Au–aerogel–CN_x, and Pt/C in Fig. 8a. As expected Pt/C exhibits HER activity with a near zero potential. The onset potential of GCE and CN_x was observed at −0.160, and −0.170 V, respectively, with very low current density. Thus it is obvious that GCE and CN_x are almost inert catalysts whereas Pt/C is an active catalyst for HER. The commercial flat Au electrode exhibits moderate HER activity with an onset potential of −150 mV. The base line corrected LSV curves for different morphologies of Au metal in the region of low current density are also presented in Fig. 8b. It clearly shows that the morphology of gold metal plays an important role in its performance towards HER activity. The porous Au–aerogel supported on CN_x sheets exhibits much better activity than AuNPs–CN_x and the flat commercial gold electrode. The onset potential for HER of Au–aerogel supported CN_x sheets is −30 mV whereas the onset potentials for AuNPs–CN_x and the flat Au electrode are −120 mV and −150 mV respectively. Under acidic conditions, the overpotentials required for Au–aerogel–CN_x to drive current densities of 10, 20 and 50 mA cm^{-2} were found to be 185, 225 and 300 mV whereas overpotentials required for AuNPs–CN are 285, 335 and 440 mV,

respectively. In contrast, flat gold shows much lower HER performances with large overpotentials of 380 and 420 mV for achieving 10 mA cm^{-2} and 20 mA cm^{-2} current density, respectively. This clearly demonstrates the superior electrocatalytic activity of Au–aerogel–CN_x towards HER. The Tafel slope is considered as an inherent property of the catalyst and used as a significant standard for the HER performance. A low Tafel slope means a faster increase of HER rate with increasing potential. The HER Tafel plots showing $\log|j|$ *vs.* applied potential for Pt/C, Au–aerogel–CN_x/GCE, AuNPs–CN_x, and AuE are given in Fig. 8c. The Tafel slope for Pt/C in acidic medium was 33 mV dec^{-1}, which is consistent with reported data. The Tafel analysis for the Au–aerogel–CN_x/GC electrode in 0.5 M H_2SO_4 gives a slope of 53 mV dec^{-1}. The Tafel slopes of the AuNPs–CN_x electrode and the commercial flat Au electrode were found to be 72 and 88 mV dec^{-1}. This low Tafel slope value (53 mV dec^{-1}) for Au–aerogel–CN_x indicates that the Volmer–Heyrovsky mechanism is responsible for the HER where the desorption of hydrogen is the rate limiting step.[79] Thus, the Tafel slope of Au–aerogel–CN_x is significantly lower than that of the flat Au electrode suggesting better HER activity on the Au–aerogel–CN_x electrode. The exchange current density for Au–aerogel–CN_x in 0.5 M H_2SO_4 medium was 0.03 mA cm^{-2} which is comparable to other related systems. The exchange current densities for the flat Au electrode and AuNPs–CN_x were found to be 0.002 and 0.004 mA cm^{-2} respectively. Another important criterion for a good HER catalyst is good stability. Stability of the catalytic responses was measured by cycling Au–aerogel–CN_x continuously for 10 000 cycles ranging from +0.8 to −0.45 V *vs.* RHE at a scan rate of 50 mV sec^{-1}. A comparison of the onset-potential, overpotential at 20 mA cm^{-2} current density, catalyst mass loading and Tafel slopes is given in Table 3. The onset potential (−30 mV) of the Au–aerogel–CN_x electrode is lower than or comparable to those of other non-platinum based systems such as Mo-based, Ni based, and Co based ones (Table 3). The required overpotential to reach a current density of 10 mA cm^{-2} for the porous Au–aerogel–CN_x is lower or the Au–aerogel–CN_x catalyst causes very little loss of cathodic current density during cycling. The long term stability of the electrode was also investigated by chronoamperometry at a fixed overpotential of −150 mV (RHE). It shows that the catalytic current density remains around 70% of the initial current density at the end of at least 10 hours (inset of Fig. 8d). The mass loading of Au in the Au–aerogel–CN_x catalyst (0.130 mg cm^{-2}) is much lower than that of previously reported catalysts. This suggests that Au–aerogel–CN_x is one of the most HER-active Pt metal-free catalyst compared to other related systems. For example FeS_2 nanosheets[83] require 265 mV to generate a current density of 10 mA cm^{-2}, Co embedded carbon rich CNTs[82] need 260 mV to generate 10 mA cm^{-2} current density, Co–MoN[84] requires 200 mV for 10 mA cm^{-2} current density, Ni_2P[42] requires 130 mV for 10 mA cm^{-2} current density and Au–aerogel–CN_x generates 10 mA cm^{-2} current density at an overpotential of 185 mV. The Tafel slope of Au–aerogel–CN_x is slightly lower than or comparable to the Tafel slope of many reported non-Pt systems (Table 3). From Table 3 it is obvious that the catalyst has comparable catalytic activity in terms of onset potential, Tafel slope, exchange current, and catalyst loading to that of other non-Pt based catalysts. In addition, some better HER performances for porous electrocatalysts are also reported in the literature. For example, Y. H. Chang *et al.*[88] reported that MoS_x film grown on graphene-protected 3D Ni foam showed high HER activity due to the highly conducting porous catalytic film. Superior catalytic behaviour was also reported for MoS_2 nanoparticles on a 3D substrate. Several groups also recently reported the morphology dependent electrocatalytic activity towards hydrogen evolution. The adhesion of the gas evolved on a flat electrode surface is a big problem because adhesion of gas bubbles blocks electrolyte diffusion leading to ohmic drop and decreases the performance of the catalyst. X. Sun and co-workers[89] demonstrated that nanostructured MoS_2 film showed much higher HER activities

Table 3 Comparison of the HER activity of different reported catalysts in acidic media

Catalyst	Catalyst loading (mg cm^{-2})	Onset potential (mV *vs.* RHE)	Overpotential (mV *vs.* RHE) *vs.* current density (mA cm^{-2})	Tafel slope (mV dec^{-1})	Exchange current (mA cm^{-2})	Ref.
$MoS_2/CoSe_2$	0.28	−11	−68 (10 mA cm^{-2})	36	0.073	80
WPNAs/CC	2	−50	−130 (10 mA cm^{-2})	69	0.29	47
MoP-CA2	0.36	−40 (IR free)	−125 (10 mA cm^{-2})	54	0.086	79
MoP	1	−50	−180 (10 mA cm^{-2})	54	0.034	46
Nano MoP	1	—	−110 (10 mA cm^{-2})	45	0.12	81
(GO 8 wt%) Cu-MOF	0.226	−87	−400 (122.48 mA cm^{-2})	84	—	34
NiP_2NS/CC	4.3	−50	−75 (10 mA cm^{-2})	51	0.26	43
Co-NRCNT	0.28	−50	−260 (10 mA cm^{-2})	69	0.01	82
$CoSe_2$	0.37	−30	−90 (4 mA cm^{-2})	40	0.037	83
$Co_{0.6}Mo_{1.4}N_2$	0.24		−200 (10 mA cm^{-2})		0.23	84
MoS_2/RGO	0.28	−100	—	−41		85
Ni_2P		−25	−130 (20 mA cm^{-2})	−46	0.033	42
CMSNA-8		−121	−365 (20 mA cm^{-2})	43	—	86
Ni–Mo–N nanosheets	0.25	−78	∼−200 mV (3.5 mA cm^{-2})	35.9	0.24	87
AuNPs–CN_x	0.127	−120	−330 (20 mA cm^{-2})	72	0.004	This work
Au–aerogel–CN_x	0.127	−30	−225 (20 mA cm^{-2})	53	0.03	This work

(overpotential, stability) than those of flat MoS_2 film due to the low gas adhesion force of the nanostructured MoS_2 electrode. Enhanced hydrogen evolution at micro and nanostructured CoS_2 as compared to flat CoS_2 film was also reported by M. S. Faber *et al.*[90] due to the enhanced release of the evolved gas from the electrode surface. The high HER activity of the Au–aerogel–CN_x catalyst could be attributed to several factors. The enhanced electrochemical surface area could be one of the reasons for superior hydrogen evolution at Au aerogel–CN_x. As discussed in the previous section, the electrochemical electrode surface area of Au–aerogel–CN_x is much higher than that of 2 nm AuNPs–CN_x or flat gold electrode. The porous network structure in Au–aerogel–CN_x is responsible for this high electrochemical surface area. It is also reported that HER activity on gold has strong structural sensitivity; the Au(111) facet is the most active for hydrogen evolution. The strong (111) reflection in p-XRD and SAED patterns (Fig. 1 and 2g) of Au–aerogel–CN_x confirmed the presence of a large amount of (111) surface sites. The HRTEM studies also suggested that the growth of the Au–aerogel occurred preferentially in (111) plane directions. The presence of a large amount of (111) planes in Au–aerogel–CN_x also suggests its high catalytic activity for HER. The strong catalyst–support interaction at Au–aerogel–CN_x may also play an important role in the superior catalytic enhancement. The strong metal–supportinteraction modifies the electronic structure of Au and carbon nitrides, which leads to fast electron transfer for catalytic reactions. The highly porous morphology of gold may enhance the mass transport to catalytic sites. Based on recent reports[88–90] on porous HER catalysts, the highly porous morphology of the Au aerogel could significantly contribute to the HER activity.

Conclusion

In conclusion, we have demonstrated a facile synthesis route for the formation of Au aerogel on carbon nitride sheets. The porous network was formed by the interconnection of AuNPs on CN_x sheets. The strong interaction between the gold aerogel and carbon nitride support, confirmed by XPS and FTIR studies, leads to changes in the electronic properties of Au and CN_x. Au–aerogel–CN_x composites have higher electrochemical surface areas and mass activities than those of AuNPs–CN_x and the commercial flat Au electrode. This catalyst exhibited superior catalytic activity towards HER and ORR. In alkaline media, the ORR activity of the Au–aerogel–CN_x catalyst is superior to that of the commercial Pt/C catalyst. The Au–CN_x composites show morphology dependent ORR and HER activities in acidic medium. The catalytic activities of the porous composite are superior to those of the AuNPs–CN_x composite and flat Au electrode. The synergistic effects between porous Au–aerogel–CN_x and carbon nitride lead to outstanding ORR and HER performances of the Au–aerogel supported on CN_x. The excellent ORR and HER activities of Au–aerogel–CN_x with methanol tolerance, good durability, and low catalyst loading make them a promising electrocatalyst for fuel cell and water splitting or other electrochemical devices.

Acknowledgements

SB thanks DST, Govt of India for financial support (project number: SR/S1/PC-10/2011). We would like to thank Prof. Shikha Varma and Mr Santosh Chowdhury (Institute of Physics, Bhubaneswar, India) for XPS measurements.

References

1 A. Corma, *Chem. Rev.*, 1997, **97**, 2373.
2 K. K. R. Datta, B. V. S. Reddy, K. Ariga and A. Vinu, *Angew. Chem., Int. Ed.*, 2010, **49**, 5961.
3 C. Xu, J. Su, X. Xu, P. Liu, H. Zhao, F. Tian and Y. Ding, *J. Am. Chem. Soc.*, 2007, **129**, 42.
4 R. Zhang, M. Hummelgård and H. Olin, *Phys. B*, 2010, **405**, 4517.
5 E. Seker, J. T. Gaskins, H. Bart-Smith, J. Zhu, M. L. Reed, G. Zangari, R. Kelly and M. R. Begley, *Acta Mater.*, 2007, **55**, 4593.
6 B. Seo and J. Kim, *Electroanalysis*, 2010, **22**, 939.
7 M. Yan, M. Zhang, S. Ge, J. Yu, M. Li, J. Huang and S. Liu, *Analyst*, 2012, **137**, 3314.
8 C. Zhu, D. Wen, M. Oschatz, M. Holzschuh, W. Liu, A.-K. Herrmann, F. Simon, S. Kaskel and A. Eychmüller, *Small*, 2015, **11**, 1430.
9 W. Liu, A.-K. Herrmann, D. Geiger, L. Borchardt, F. Simon, S. Kaskel, N. Gaponik and A. Eychmüller, *Angew. Chem.*, 2012, **124**, 5841.
10 S. S. Kistler, *Nature*, 1931, **127**, 741.
11 A. G. Sadekar, S. S. Mahadik, A. N. Bang, Z. J. Larimore, C. A. Wisner, M. F. Bertino, A. K. Kalkan, J. T. Mang, C. Sotiriou-Leventis and N. Leventis, *Chem. Mater.*, 2012, **24**, 26.
12 A. Soleimani Dorcheh and M. H. Abbasi, *J. Mater. Process. Technol.*, 2008, **199**, 10.
13 F. Hoffmann, M. Cornelius, J. Morell and M. Fröba, *Angew. Chem., Int. Ed.*, 2006, **45**, 3216.
14 F. J. Heiligtag, W. Cheng, V. R. de Mendonça, M. J. Süess, K. Hametner, D. Günther, C. Ribeiro and M. Niederberger, *Chem. Mater.*, 2014, **26**, 5576.
15 J. L. Mohanan, I. U. Arachchige and S. L. Brock, *Science*, 2005, **307**, 397.
16 N. C. Bigall, A.-K. Herrmann, M. Vogel, M. Rose, P. Simon, W. Carrillo-Cabrera, D. Dorfs, S. Kaskel, N. Gaponik and A. Eychmüller, *Angew. Chem., Int. Ed.*, 2009, **48**, 9731.
17 N. Leventis, N. Chandrasekaran, C. Sotiriou-Leventis and A. Mumtaz, *J. Mater. Chem.*, 2009, **19**, 63.
18 N. Leventis, N. Chandrasekaran, A. G. Sadekar, S. Mulik and C. Sotiriou-Leventis, *J. Mater. Chem.*, 2010, **20**, 7456.
19 B. C. Tappan, M. H. Huynh, M. A. Hiskey, D. E. Chavez, E. P. Luther, J. T. Mang and S. F. Son, *J. Am. Chem. Soc.*, 2006, **128**, 6589.
20 A. Corma and H. Garcia, *Chem. Soc. Rev.*, 2008, **37**, 2096.
21 A. A. Herzing, C. J. Kiely, A. F. Carley, P. Landon and G. J. Hutchings, *Science*, 2008, **321**, 1331.
22 B. Yoon, H. Häkkinen, U. Landman, A. S. Wörz, J.-M. Antonietti, S. Abbet, K. Judai and U. Heiz, *Science*, 2005, **307**, 403.

23 B. E. Hayden, D. Pletcher and J.-P. Suchsland, *Angew. Chem., Int. Ed.*, 2007, **46**, 3530.
24 A. K. Geim, *Science*, 2009, **324**, 1530.
25 J. Liu, H. Bai, Y. Wang, Z. Liu, X. Zhang and D. D. Sun, *Adv. Funct. Mater.*, 2010, **20**, 4175.
26 T. Bhowmik, M. K. Kundu and S. Barman, *RSC Adv.*, 2015, **5**, 38760.
27 X. Yao, X. Liu and X. Hu, *ChemCatChem*, 2014, **6**, 3409.
28 G. M. Scheuermann, L. Rumi, P. Steurer, W. Bannwarth and R. Mülhaupt, *J. Am. Chem. Soc.*, 2009, **131**, 8262.
29 S. Guo, D. Wen, Y. Zhai, S. Dong and E. Wang, *ACS Nano*, 2010, **4**, 3959.
30 M. K. Kundu, M. Sadhukhan and S. Barman, *J. Mater. Chem. B*, 2015, **3**, 1289.
31 W. Liu, P. Rodriguez, L. Borchardt, A. Foelske, J. Yuan, A.-K. Herrmann, D. Geiger, Z. Zheng, S. Kaskel, N. Gaponik, R. Kötz, T. J. Schmidt and A. Eychmüller, *Angew. Chem., Int. Ed.*, 2013, **52**, 9849.
32 J. Zhang, Y. Xu and B. Zhang, *Chem. Commun.*, 2014, **50**, 13451.
33 W. Liu, A.-K. Herrmann, D. Geiger, L. Borchardt, F. Simon, S. Kaskel, N. Gaponik and A. Eychmüller, *Angew. Chem., Int. Ed.*, 2012, **51**, 5743.
34 M. Jahan, Z. Liu and K. P. Loh, *Adv. Funct. Mater.*, 2013, **23**, 5363.
35 W. Sheng, M. Myint, J. G. Chen and Y. Yan, *Energy Environ. Sci.*, 2013, **6**, 1509.
36 Y. Wang, E. Laborda, K. Tschulik, C. Damm, A. Molina and R. G. Compton, *Nanoscale*, 2014, **6**, 11024.
37 Y. Wang, E. Laborda, K. R. Ward, K. Tschulik and R. G. Compton, *Nanoscale*, 2013, **5**, 9699.
38 M. Bron, *J. Electroanal. Chem.*, 2008, **624**, 64.
39 T. Inasaki and S. Kobayashi, *Electrochim. Acta*, 2009, **54**, 4893.
40 S. Guerin, B. E. Hayden, D. Pletcher, M. E. Rendall and J.-P. Suchsland, *J. Comb. Chem.*, 2006, **8**, 679.
41 L. Liao, J. Zhu, X. Bian, L. Zhu, M. D. Scanlon, H. H. Girault and B. Liu, *Adv. Funct. Mater.*, 2013, **23**, 5326.
42 E. J. Popczun, J. R. McKone, C. G. Read, A. J. Biacchi, A. M. Wiltrout, N. S. Lewis and R. E. Schaak, *J. Am. Chem. Soc.*, 2013, **135**, 9267.
43 P. Jiang, Q. Liu and X. Sun, *Nanoscale*, 2014, **6**, 13440.
44 W. F. Chen, C. H. Wang, K. Sasaki, N. Marinkovic, W. Xu, J. T. Muckerman, Y. Zhu and R. R. Adzic, *Energy Environ. Sci.*, 2013, **6**, 943.
45 H. Vrubel and X. Hu, *Angew. Chem., Int. Ed.*, 2012, **51**, 12703.
46 P. Xiao, M. A. Sk, L. Thia, X. Ge, R. J. Lim, J.-Y. Wang, K. H. Lim and X. Wang, *Energy Environ. Sci.*, 2014, **7**, 2624.
47 Z. Pu, Q. Liu, A. M. Asiri and X. Sun, *ACS Appl. Mater. Interfaces*, 2014, **6**, 21874.
48 M. A. Lukowski, A. S. Daniel, C. R. English, F. Meng, A. Forticaux, R. J. Hamers and S. Jin, *Energy Environ. Sci.*, 2014, **7**, 2608.
49 Y. Xu, *Int. J. Electrochem. Sci.*, 2009, **34**, 77.
50 R. Creţu, A. Kellenberger, M. Medeleanu and N. Vaszilcsin, *Int. J. Electrochem. Sci.*, 2014, **9**, 4465.
51 J. Perez and E. R. Gonzalez, *J. Phys. Chem. B*, 1998, **102**, 10931.
52 S. Barman and M. Sadhukhan, *J. Mater. Chem.*, 2012, **22**, 21832.
53 M. Sadhukhan and S. Barman, *J. Mater. Chem. A*, 2013, **1**, 2752.
54 N. Cheng, J. Tian, Q. Liu, C. Ge, A. H. Qusti, A. M. Asiri, A. O. Al-Youbi and X. Sun, *ACS Appl. Mater. Interfaces*, 2013, **5**, 6815.
55 C. D. Wagner and G. E. Muilenberg, *Handbook of X-ray Photoelectron Spectroscopy: a Reference Book of Standard Data for Use in X-ray Photoelectron Spectroscopy*, Physical Electronics Division, Perkin-Elmer Corp., 1979.
56 M. Sadhukhan, T. Bhowmik, M. K. Kundu and S. Barman, *RSC Adv.*, 2014, **4**, 4998.
57 L. Tang, Y. Wang, Y. Li, H. Feng, J. Lu and J. Li, *Adv. Funct. Mater.*, 2009, **19**, 2782.
58 H. Erikson, A. Sarapuu, K. Tammeveski, J. Solla-Gullón and J. M. Feliu, *ChemElectroChem*, 2014, **1**, 1338.
59 H. S. Wroblowa, P. Yen Chi and G. Razumney, *J. Electroanal. Chem.Interface. Electrochem.*, 1976, **69**, 195.
60 J. Hernández, J. Solla-Gullón and E. Herrero, *J. Electroanal. Chem.*, 2004, **574**, 185.
61 C. M. Sánchez-Sánchez, F. J. Vidal-Iglesias, J. Solla-Gullón, V. Montiel, A. Aldaz, J. M. Feliu and E. Herrero, *Electrochim. Acta*, 2010, **55**, 8252.
62 R. R. Adić, N. M. Marković and V. B. Vešović, *J. Electroanal. Chem.*, 1984, **165**, 105.
63 A. I. Gopalan, K.-P. Lee, K. M. Manesh, P. Santhosh and J. H. Kim, *J. Mol. Catal. A: Chem.*, 2006, **256**, 335.
64 H. Erikson, G. Jürmann, A. Sarapuu, R. J. Potter and K. Tammeveski, *Electrochim. Acta*, 2009, **54**, 7483.
65 M. S. El-Deab, T. Sotomura and T. Ohsaka, *Electrochem. Commun.*, 2005, **7**, 29.
66 E. Negro, S. Polizzi, K. Vezzù, L. Toniolo, G. Cavinato and V. Di Noto, *Int. J. Hydrogen Energy*, 2014, **39**, 2828.
67 V. Di Noto, E. Negro, S. Polizzi, P. Riello and P. Atanassov, *Appl. Catal., B*, 2012, **111–112**, 185.
68 S. Yang, X. Feng, X. Wang and K. Müllen, *Angew. Chem., Int. Ed.*, 2011, **50**, 5339.
69 A. Sarapuu, K. Tammeveski, T. T. Tenno, V. Sammelselg, K. Kontturi and D. J. Schiffrin, *Electrochem. Commun.*, 2001, **3**, 446.
70 H. Yin, C. Zhang, F. Liu and Y. Hou, *Adv. Funct. Mater.*, 2014, **24**, 2930.
71 B. K. Barman and K. K. Nanda, *Chem. Commun.*, 2013, **49**, 8949.
72 H. Zhu, S. Zhang, Y.-X. Huang, L. Wu and S. Sun, *Nano Lett.*, 2013, **13**, 2947.
73 G. Zhang, S. Sun, M. Cai, Y. Zhang, R. Li and X. Sun, *Sci. Rep.*, 2013, **3**, 1526.
74 M. Haruta, *Faraday Discuss.*, 2011, **152**, 11.
75 E. Negro, K. Vezzù, F. Bertasi, P. Schiavuta, L. Toniolo, S. Polizzi and V. Di Noto, *ChemElectroChem*, 2014, **1**, 1359.
76 V. Di Noto, E. Negro, S. Polizzi, F. Agresti and G. A. Giffin, *ChemSusChem*, 2012, **5**, 2451.
77 V. Di Noto and E. Negro, *Fuel Cells*, 2010, **10**, 234.
78 L. Perini, C. Durante, M. Favaro, V. Perazzolo, S. Agnoli, O. Schneider, G. Granozzi and A. Gennaro, *ACS Appl. Mater. Interfaces*, 2015, **7**, 1170.

79 Z. Xing, Q. Liu, A. M. Asiri and X. Sun, *Adv. Mater.*, 2014, **26**, 5702.
80 M.-R. Gao, J.-X. Liang, Y.-R. Zheng, Y.-F. Xu, J. Jiang, Q. Gao, J. Li and S.-H. Yu, *Nat. Commun.*, 2015, **6**, 5982.
81 J. M. McEnaney, J. C. Crompton, J. F. Callejas, E. J. Popczun, A. J. Biacchi, N. S. Lewis and R. E. Schaak, *Chem. Mater.*, 2014, **26**, 4826.
82 X. Zou, X. Huang, A. Goswami, R. Silva, B. R. Sathe, E. Mikmeková and T. Asefa, *Angew. Chem., Int. Ed.*, 2014, **126**, 4461.
83 D. Kong, J. J. Cha, H. Wang, H. R. Lee and Y. Cui, *Energy Environ. Sci.*, 2013, **6**, 3553.
84 B. Cao, G. M. Veith, J. C. Neuefeind, R. R. Adzic and P. G. Khalifah, *J. Am. Chem. Soc.*, 2013, **135**, 19186.
85 Y. Li, H. Wang, L. Xie, Y. Liang, G. Hong and H. Dai, *J. Am. Chem. Soc.*, 2011, **133**, 7296.
86 H. Yu, X. Yu, Y. Chen, S. Zhang, P. Gao and C. Li, *Nanoscale*, 2015, **7**, 8731.
87 W.-F. Chen, K. Sasaki, C. Ma, A. I. Frenkel, N. Marinkovic, J. T. Muckerman, Y. Zhu and R. R. Adzic, *Angew. Chem., Int. Ed.*, 2012, **51**, 6131.
88 Y.-H. Chang, C.-T. Lin, T.-Y. Chen, C.-L. Hsu, Y.-H. Lee, W. Zhang, K.-H. Wei and L.-J. Li, *Adv. Mater.*, 2013, **25**, 756.
89 Z. Lu, W. Zhu, X. Yu, H. Zhang, Y. Li, X. Sun, X. Wang, H. Wang, J. Wang, J. Luo, X. Lei and L. Jiang, *Adv. Mater.*, 2014, **26**, 2683.
90 M. S. Faber, R. Dziedzic, M. A. Lukowski, N. S. Kaiser, Q. Ding and S. Jin, *J. Am. Chem. Soc.*, 2014, **136**, 10053.